CHAPTER IV

RESULTS AND DISCUSSION

4.1 Precipitation of Iron Oxide from the Industrial Iron Waste Solution

Iron oxide precipitated from the industrial iron waste has reddish-orange color and XRD structure is shown in Figure 4.1. The amount of iron and other elements were analyzed by XRF. It has been concluded that the product are mainly composed of 95.14 % Fe_2O_3 and small amount of 0.34% Na_2O, 0.12% Al_2O_3, 0.11% SiO_2, 0.65% P_2O_5, 0.01% SO_3, 2.59% Cl, 0.02% V_2O_5, 0.41% Cr_2O_3, and 0.61% ZnO.

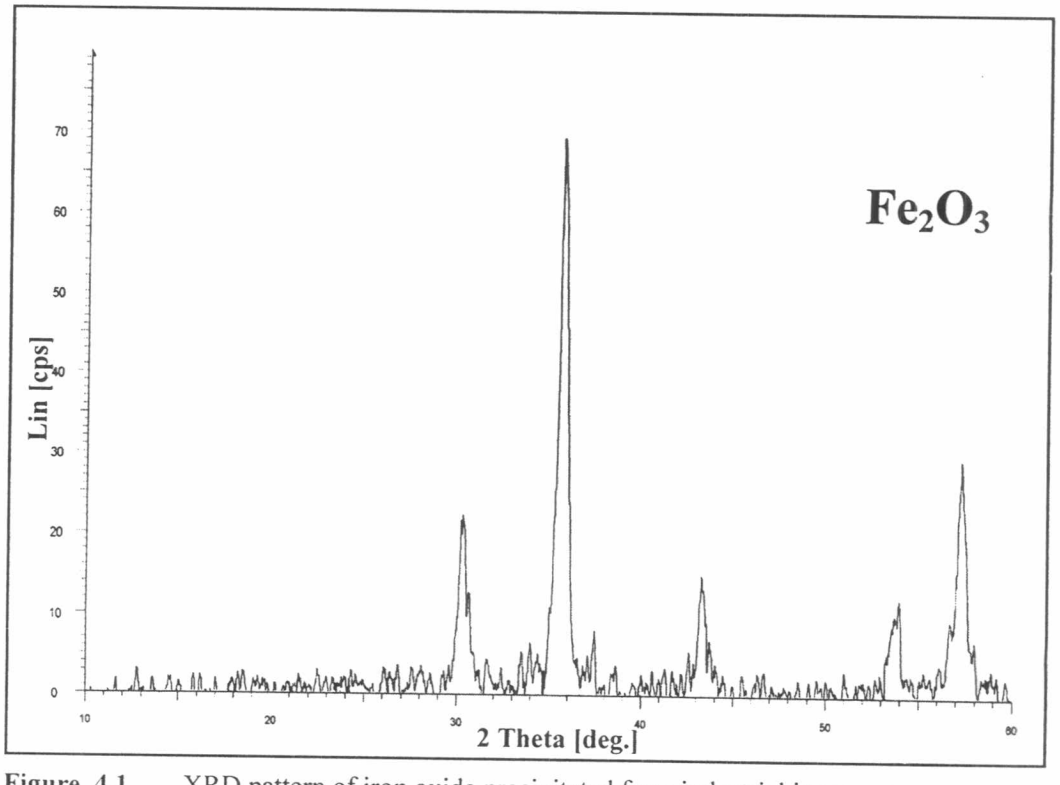

Figure 4.1 XRD pattern of iron oxide precipitated from industrial iron waste

4.2 Characterization of Fe-MCM-41

4.2.1 Structural Characterization of Fe-MCM-41

XRD patterns of as-synthesized samples prepared by one-step and two-step crystallization methods are compared in Figure 4.2. The sample synthesized using two-step crystallizations shows the four characteristic peaks of d_{100}, d_{110}, d_{200}, and d_{210}, which can be indicated to a hexagonal pore structure of MCM-41 material while the sample synthesized using one step crystallization exhibits a disorder of the pore structure. Acetic acid added to the gel mixture to adjust pH during crystallization step is proposed to play an important role for neutralizing hydroxyl groups of the product. Therefore, the condensation of the gel mixture is increased. [69]

Moreover, XRD patterns of as-synthesized samples with the Si/Fe ratios in the gel of 30, 40, 50, and 100 are displayed in Figure 4.3. The XRD patterns of samples with the Si/Fe ratios of 50 and 100 exhibit four characteristic peaks of the MCM-41 structure while those of samples with the Si/Fe ratios of 30 and 40 show disorder of the pore structure. It has been suggested that large atomic radius of iron in the framework makes the hexagonal pore structure collapsed causing disorder of reflection lines. Beside, the framework structure of Fe-MCM-41 does not depended on the aging time of the synthesis gel, e.g. the as-synthesized samples with Si/Fe ratio of 30, D and E have similar disorder of the hexagonal pore structure.

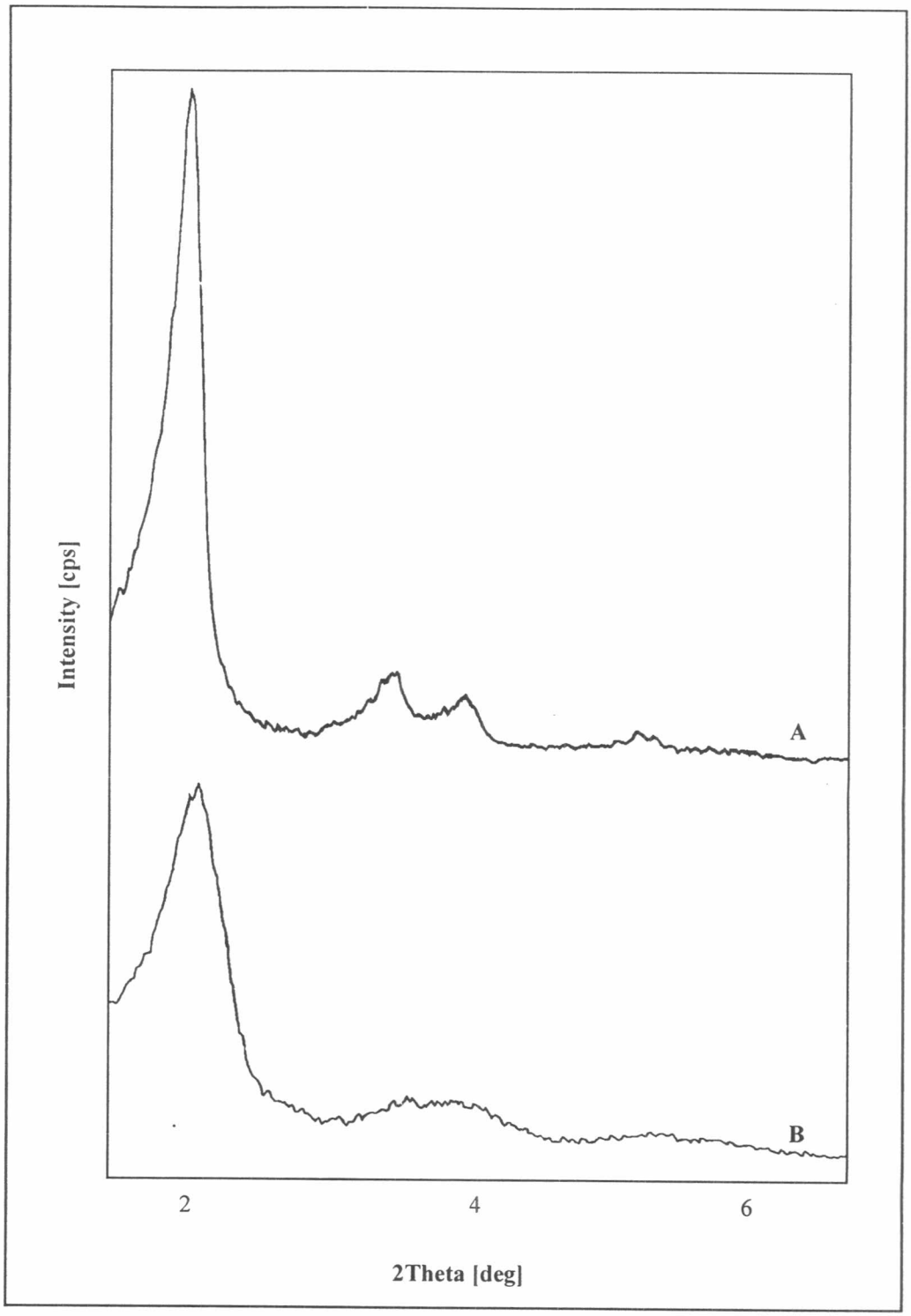

Figure 4.2 XRD patterns of as-synthesized samples with Si/Fe = 50; (A) Fe-MCM-41-N3 (two-step crystallization) and (B) Fe-MCM-41-OS (one-step crystallization).

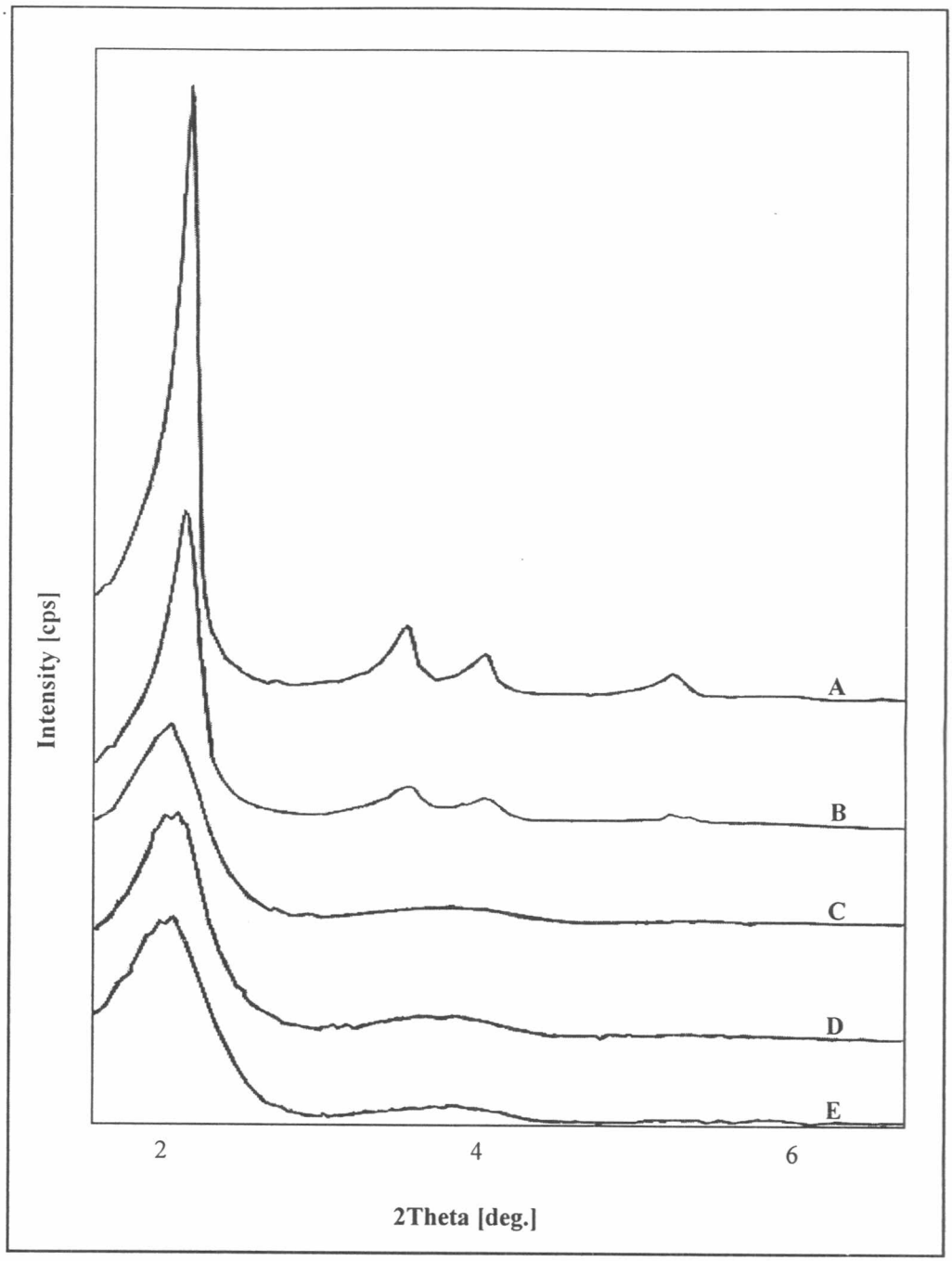

Figure 4.3 XRD patterns of as-synthesized samples with different Si/Fe ratios; (A) Fe-MCM-41-N6 (Si/Fe = 100), (B) Fe-MCM-41-N4 (Si/Fe = 50), (C) Fe-MCM-41-N2 (Si/Fe = 40), (D) Fe-MCM-41-N1 (Si/Fe = 30) and, (E) Fe-MCM-41-OV24H (Si/Fe = 30). Gel mixture of sample E was aged at room temperature for 24 hours before hydrothermal crystallization.

For synthesis of Fe-MCM-41 using iron oxide waste as the iron source, the XRD patterns of as-synthesized and calcined Fe-MCM-41-NW4 are shown in Figure 4.4. Both samples show four characteristic peaks of the hexagonal pore structure but intensity of the d_{100} peak of the calcined sample is higher than that of the as-synthesized sample, which refers to thermal stability of the sample.

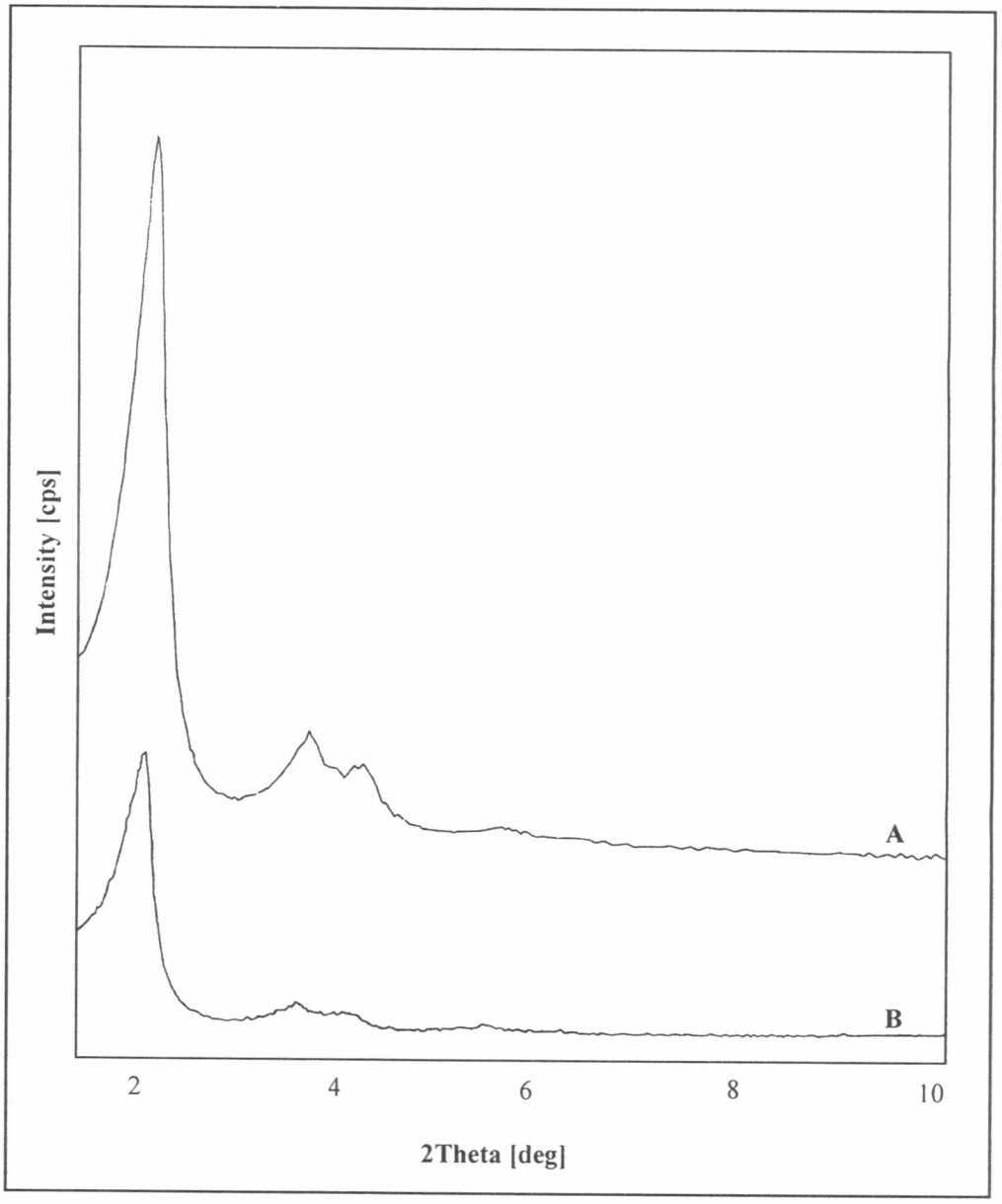

Figure 4.4 XRD patterns of Fe-MCM-41-NW4 with Si/Fe = 50, synthesized using iron oxide waste; (A) Calcined sample and (B) As-synthesized sample.

4.2.2 Determination of Iron Content in Fe-MCM-41

AAS technique is used to determine the iron content in the Fe-MCM-41 samples. Table 4.1 shows the iron content in forms of Fe_2O_3 and the Si/Fe ratios in the synthesis gel comparing with those of the calcined Fe-MCM-41 sample. The results showed that the Si/Fe ratios of calcined samples are lower than those in gel. It can be described that Fe^{3+} ions have a good ability to replace silicon in the framework. However, the effect of aging time for gels with Si/Fe ratio of 50 is observed, e.g. Fe-MCM-41-N3 and Fe-MCM-41-N4. Sample with aging time of 30 minutes has Si/Fe ratio in calcined sample higher than in gel. Moreover, the sample with the Si/Fe ratio in gel of 30 has the highest iron content, but the XRD pattern in Figure 4.3 does not represent the hexagonal pore structure. Therefore, it can be summarized that the amount of iron containing in Fe-MCM-41 is depended on aging time, the amount of iron in the gel, and the Si/Fe ratio. The maximum Si/Fe ratio of Fe-MCM-41 synthesized by this procedure is limited at 50.

Table 4.1 The iron content and Si/Fe ratios in the calcined Fe-MCM-41 sample compared with Si/Fe ratios in gel.

Samples	Aging time (hour)	Si/Fe ratio in gels	Si/Fe ratio in calcined samples	%wt. Fe_2O_3 in calcined samples
Fe-MCM-41-N1	2	30	26.66	4.74
Fe-MCM-41-N3	0.5	50	55.67	2.33
Fe-MCM-41-N4	2	50	46.30	2.78
Fe-MCM-41-N5	2	50	45.19	2.85
Fe-MCM-41-NW4	2	50	44.90	2.87
Fe-MCM-41-N6	2	100	85.01	1.54

4.2.3 Identification of the Iron Location in the Fe-MCM-41 Structure

ESR is the specific technique to identify the location of iron species in many materials. From Figure 4.5, all Fe-MCM-41 samples have two ESR signals at g = 5.0 and 2.0. The signals at g = 5.0 are assigned for tetrahedral coordination of iron in the framework and the signals at g = 2.0 are assigned for octahedral coordination of iron in the extra-framework sites. The ESR spectra of ferric oxide is used for confirming the octahedral coordination of iron at g = 2.0. Generally, the signals at g = 4.2 - 4.3 are assigned for tetrahedral coordination of iron, but the signal at g = 5.0 is observed in this study. To confirm the signal at g = 5.0 as the tetrahedral coordination of iron, the ESR signals of as-synthesized and calcined samples are compared. The strong signal at g = 5.0 is observed in the as-synthesized sample. After calcination, the intensity of the signal at g = 5.0 is decreased because iron species in tetrahedral sites are oxidized and converted to octahedral coordination during the calcination process. The relative intensities of ESR signals of Fe-MCM-41 samples are summarized in Table 4.2. It is clearly seen that the number of iron atoms in octahedral sites increases when the amount of iron is raised. These results are in agreement with the results reported by He, N.Y.et. al.[35] Their ESR results showed that the number of octahedral iron is increased with increasing in iron content, calcination time and temperature.

Table 4.2 Relative intensity of ESR signals of Fe-MCM-41 samples

Sample	Relative intensity		Si/Fe	Si/Fe	Si/Fe_{Oh}	Si/Fe_{Td}
	g = 2.0	g = 5.0	in gel	in product	(x 10^{-2})	(x 10^{-2})
cal- Fe-MCM-41-NW4	1544	248	50	44.9	2.91	18.10
cal- Fe-MCM-41-N3	1086	106	50	55.7	5.13	52.52
cal- Fe-MCM-41-N6	364	143	100	85.0	23.35	59.45

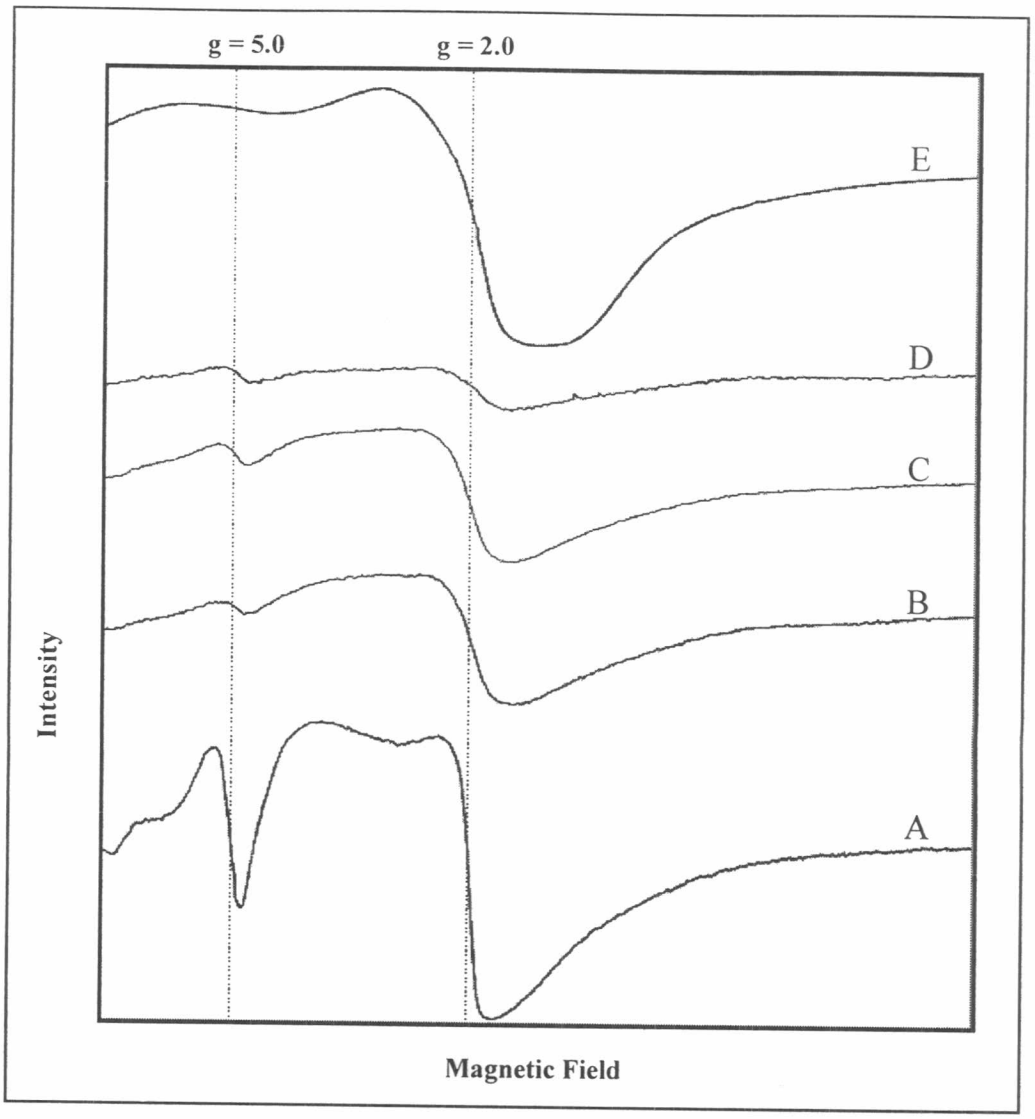

Figure 4.5 ESR spectra of Fe-MCM-41 and ferric oxide; (A) As-synthesized Fe-MCM-41-N3 (Si/Fe = 50), (B) Calcined Fe-MCM-41-N3 (Si/Fe = 50), (C) Calcined Fe-MCM-41-NW4 (Si/Fe = 50), (D) Calcined Fe-MCM-41-N6 (Si/Fe = 100) and (E) Ferric oxide.

4.2.4 Scanning Electron Microscope of Fe-MCM-41

SEM images of as-synthesized samples of Fe-MCM-4-N4 and Fe-MCM-41-NW4 are shown in Figure 4.6 and 4.7, respectively. Worm-like particles are observed from Fe-MCM-4-NW4 with a smaller size. Conversely, Fe-MCM-41-N4 exhibits rod shape

particles. The differences in particle size and shape morphology between Fe-MCM-41-N4 and Fe-MCM-41-NW4 samples may be due to the anion effect.[25] The iron solution for Fe-MCM-41-NW4 was prepared in nitric acid, while for Fe-MCM41-N4 was prepared using sulfuric acid.

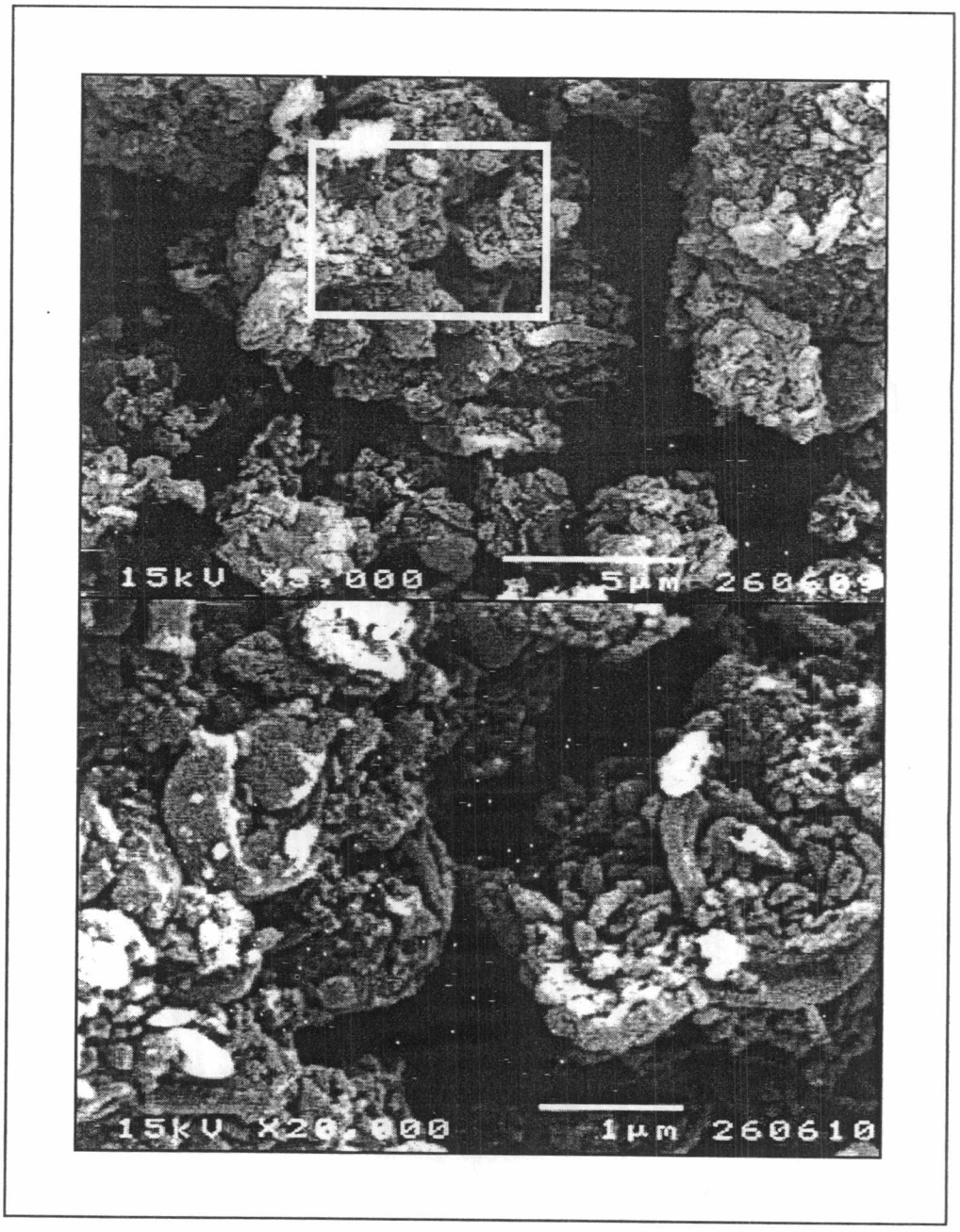

Figure 4.6 SEM image of as-synthesized Fe-MCM-41-N4 (Si/Fe = 50)

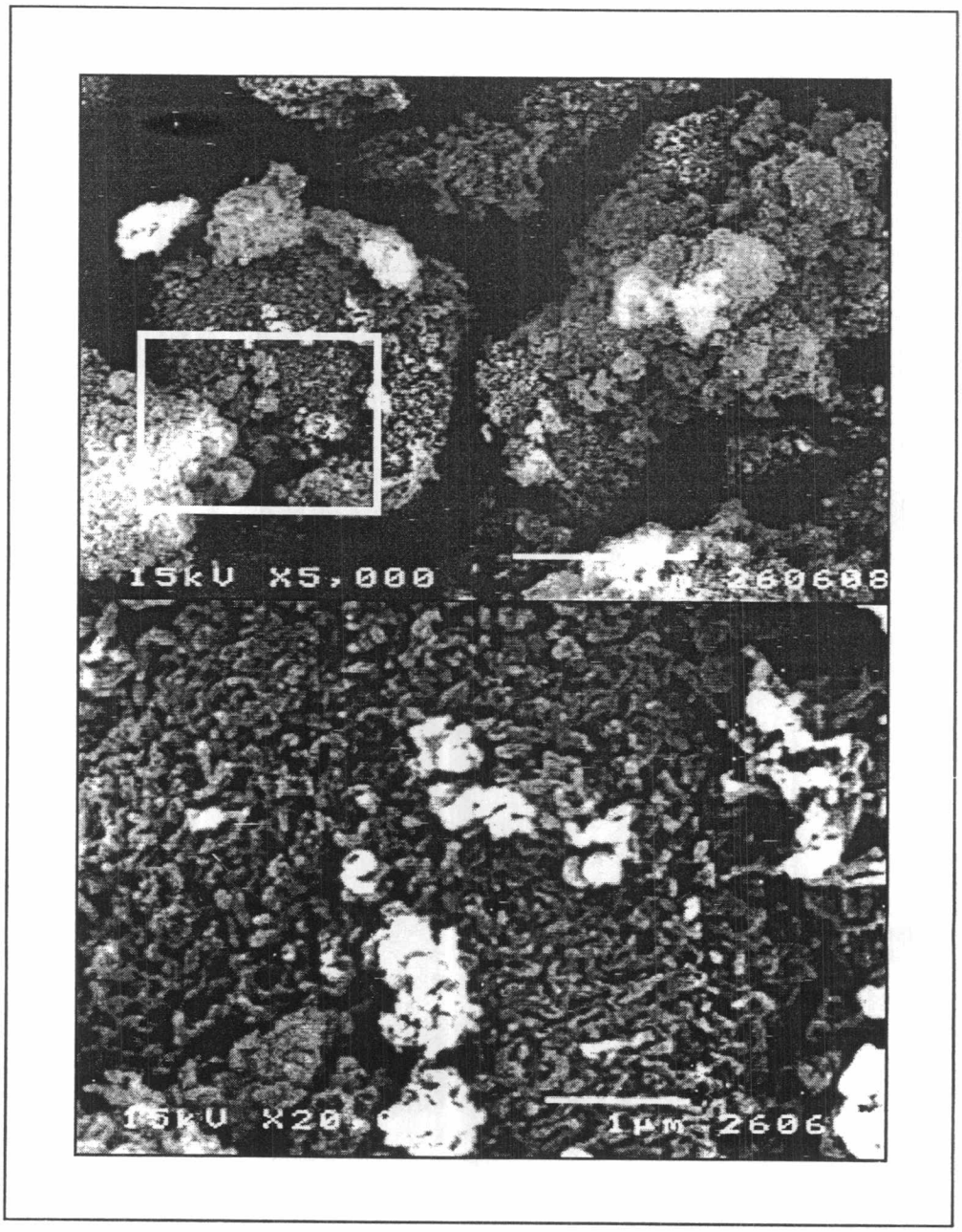

Figure 4.7 SEM image of as-synthesized Fe-MCM-41-NW4 (Si/Fe = 50)

4.2.5 Nitrogen Adsorption-desorption Measurement

This technique is very useful for determination of pore sizes, pore volumes, and surface area of porous materials. The pore volume, pore size and BET specific surface areas of the samples are concluded in Table 4.3. The BET specific surface area of Fe-MCM-41-N4 is slightly lower than Fe-MCM-41-NW4 because of the larger particle size (see Figure 4.6 and 4.7) and larger pore volume of Fe-MCM-41-NW4. Nitrogen adsorption-desorption isotherms and pore size distribution of calcined Fe-MCM-41-NW4 and Fe-MCM-41-N4 are shown in Figure 4.8 and 4.9, respectively. The reversible type IV isotherms are observed for both samples indicating the mesopore structure of the samples and uniform pore size distribution in the range of 2.8 – 3.2 nm.

Table 4.3 Specific surface area, pore volume, and pore diameter of Fe-MCM-41 samples

Sample	BET surface area (m^2/g)	BJH pore volume (cm^3/g)	BJH pore diameter (nm)
Fe-MCM-41-NW4	889.45	0.93	3.12
Fe-MCM-41-N4	836.45	0.92	2.94

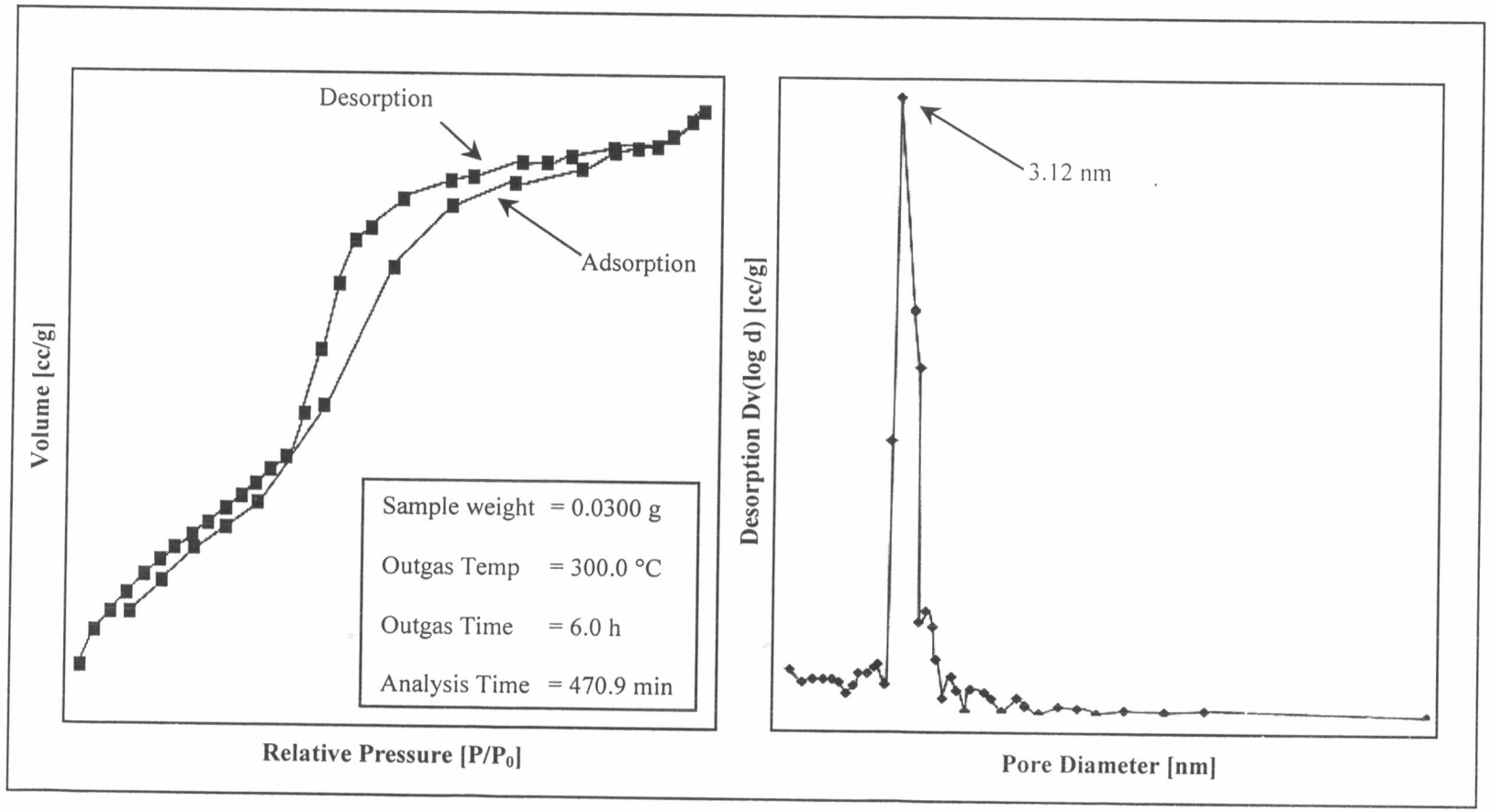

Figure 4.8 N_2 adsorption-desorption isotherm and pore sizes distribution of Fe-MCM-41-NW4

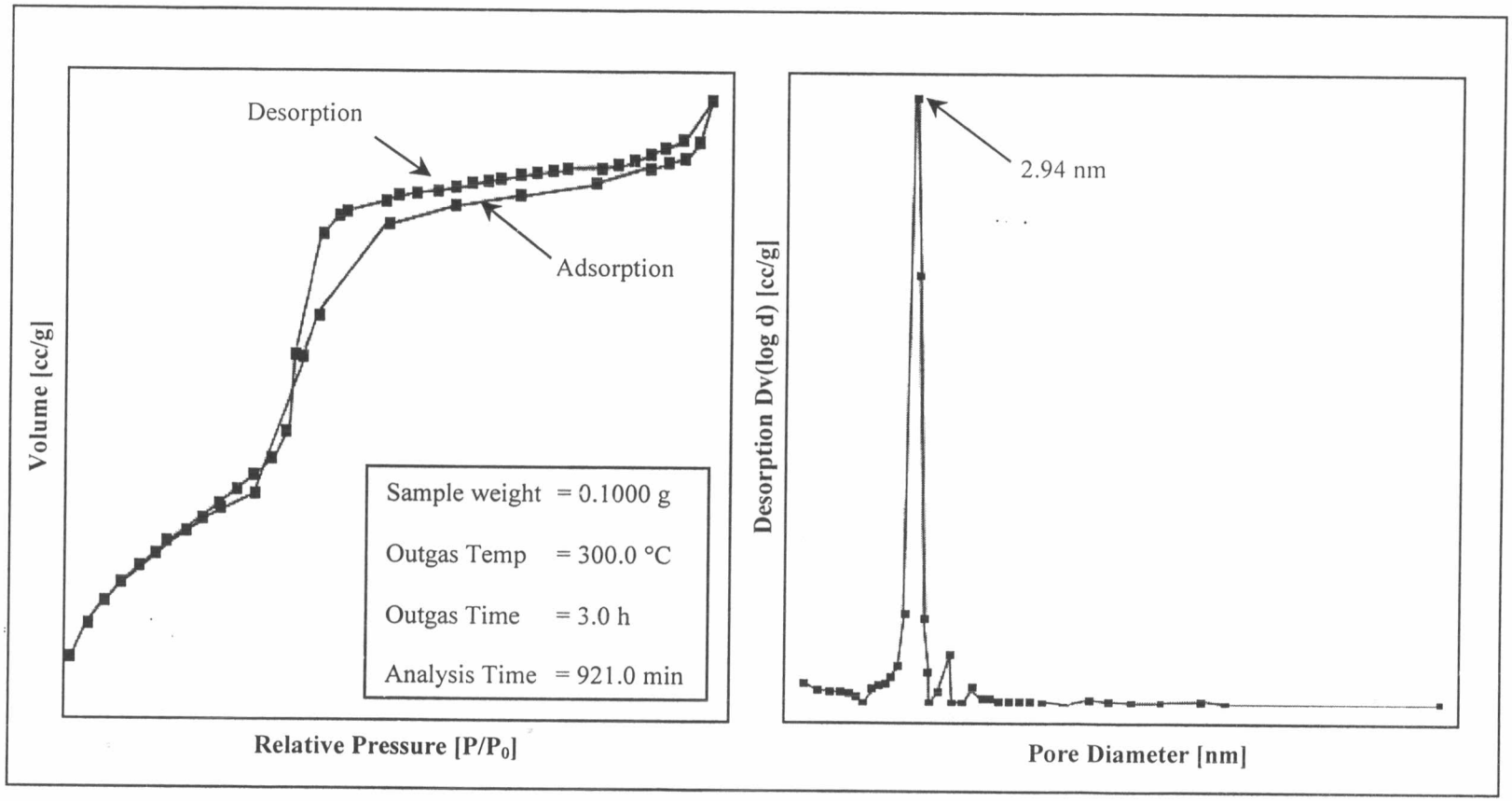

Figure 4.9 N_2 adsorption-desorption isotherm and pore sizes distribution of Fe-MCM-41-N4

4.3 Catalytic Activity of Fe-MCM-41 in Friedel-Crafts Alkylation.

4.3.1 Arylation of Benzene with Benzyl Chloride Over Fe-MCM-41 Catalysts

Arylation of benzene with benzyl chloride is used for studying the catalytic activity of Fe-MCM-41-NW4 and Fe-MCM-41-N4. The results from Fe-MCM-41-NW4 are similar to those of Fe-MCM-41-N4. Conversions of benzyl chloride at different reaction conditions for both catalysts are shown in Figure 4.10A and 4.11B. It has been seen that the conversion is increased with increasing reaction time and temperature. At 40 °C, conversion of benzyl chloride is not observed eventhough the reaction time is increased from 1 hour to 2 and 4 hours. At the temperature of 50 °C, benzyl chloride reacts with benzene in a period of 4 hours and gives conversion around 10-11%. The conversions higher than 99 % are observed when the reaction temperature is raised to 60 and 100 °C for 2 - 4 hours.

The products from arylation of benzene are mostly diphenylmethane and minor amount of dibenzylbenzene. The selectivity to main product, diphenylmethane, is also increased with increasing reaction temperature, as showed in Figure 4.10B and 4.11B. The highest selectivity is found when the reaction is performed at 100 °C for 1 hour. However, the selectivity is decreased when the reaction time increases. It can be described that arylation of benzene to produce diphenylmethane molecules is parallel to polyarylation of benzyl chloride producing dibenzylbenzene by product. The mass spectrum of diphenylmethane analyzed by GC-MS is given in Figure 4.12. The parents peak observed at m/z = 78.62 in Figure 4.12A is the ion of benzene molecule reactant. Figure 4.12B shows the parents and fragment peaks at m/z = 167.16 and 90.19, respectively. The parents peak at m/z = 167.16 can be assigned to the cation of diphenylmethane and the fragment at m/z = 90.16 can be assigned for the benzyl cation.

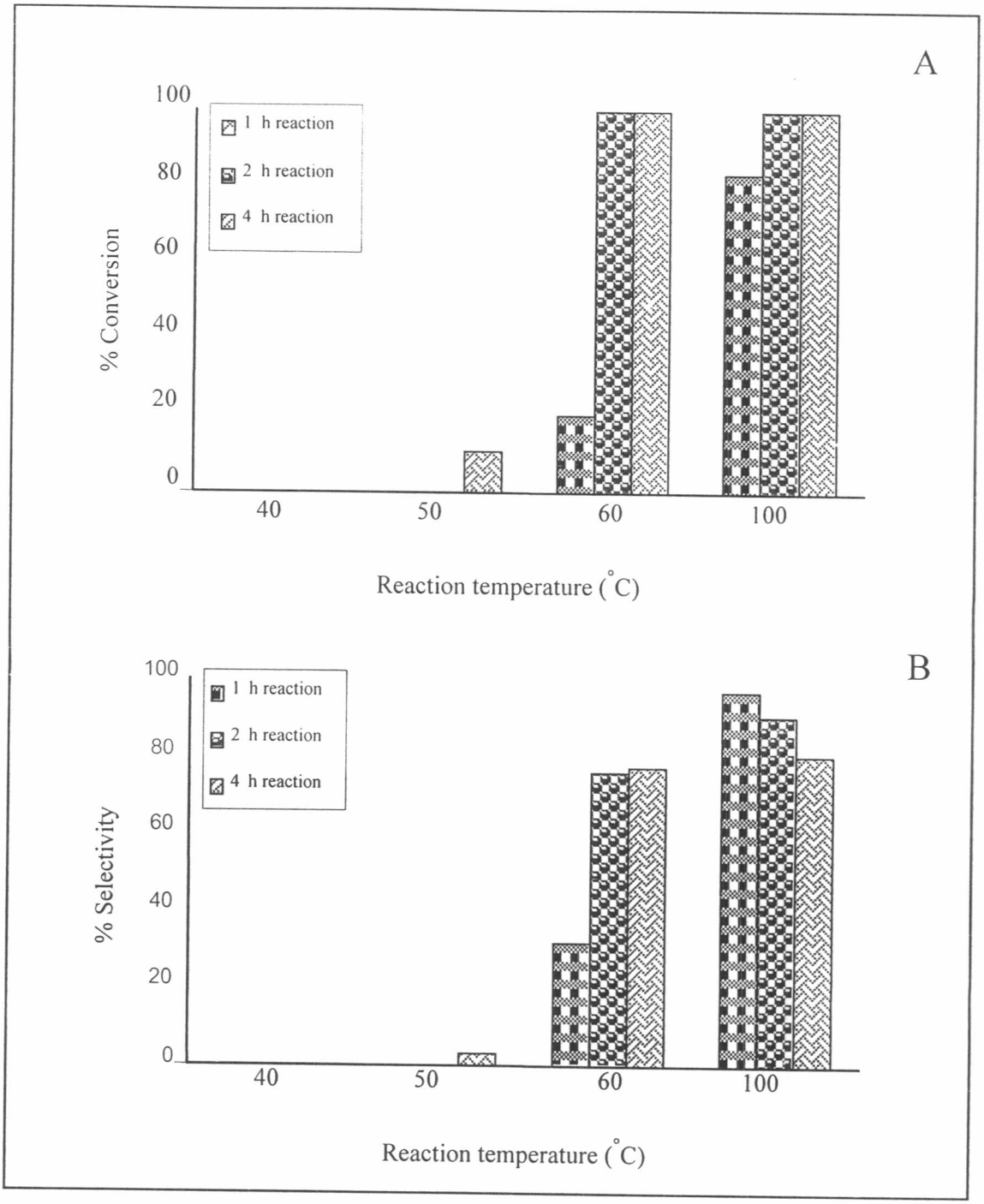

Figure 4.10 Catalytic activity of Fe-MCM-41-NW4 in arylation of benzene with benzyl chloride, (A) Conversion of benzyl chloride and (B) Selectivity to diphenylmethane

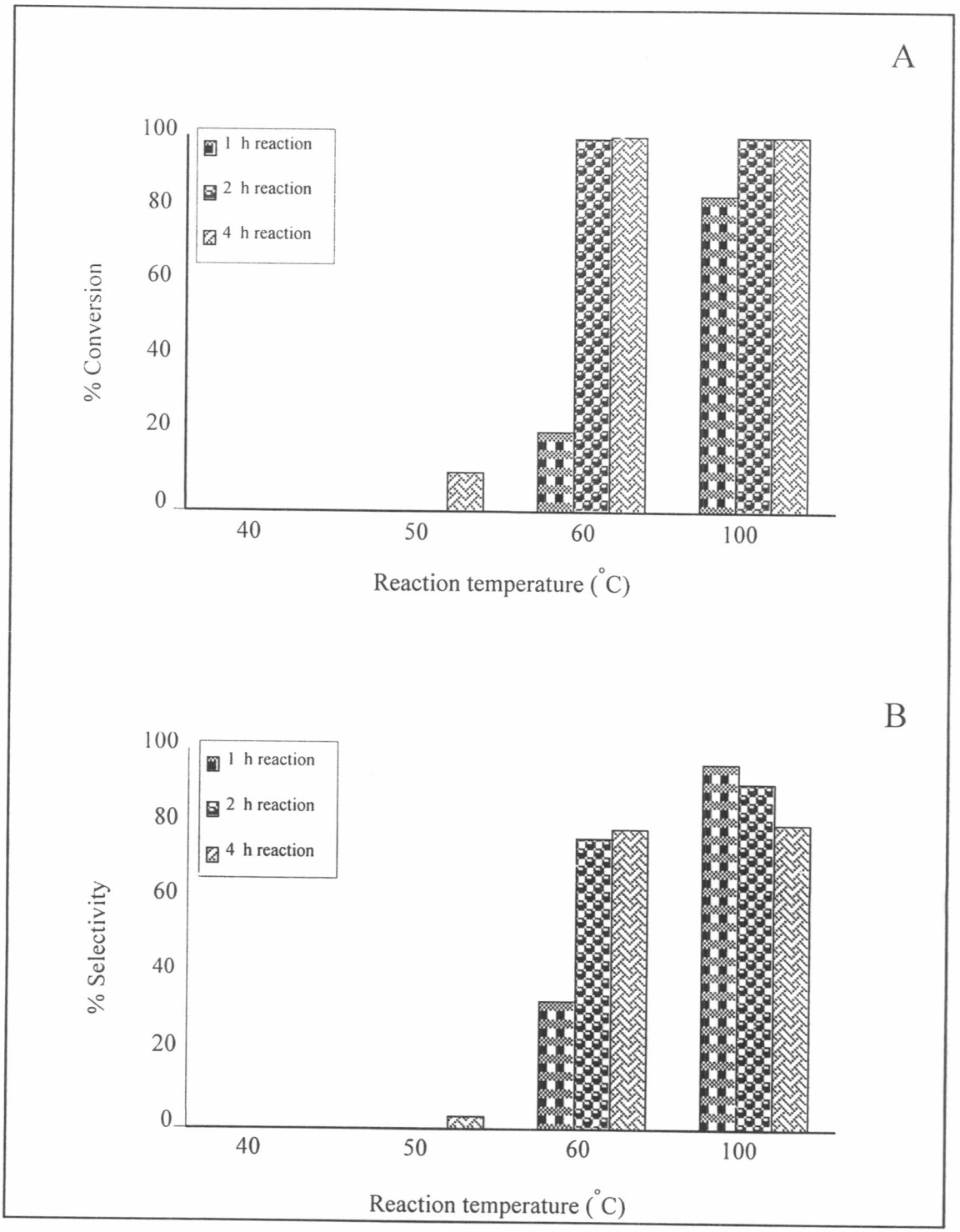

Figure 4.11 Catalytic activity of Fe-MCM-41-N4 in arylation of benzene with benzyl chloride, (A) Conversion of benzyl chloride and (B) Selectivity to diphenylmethane

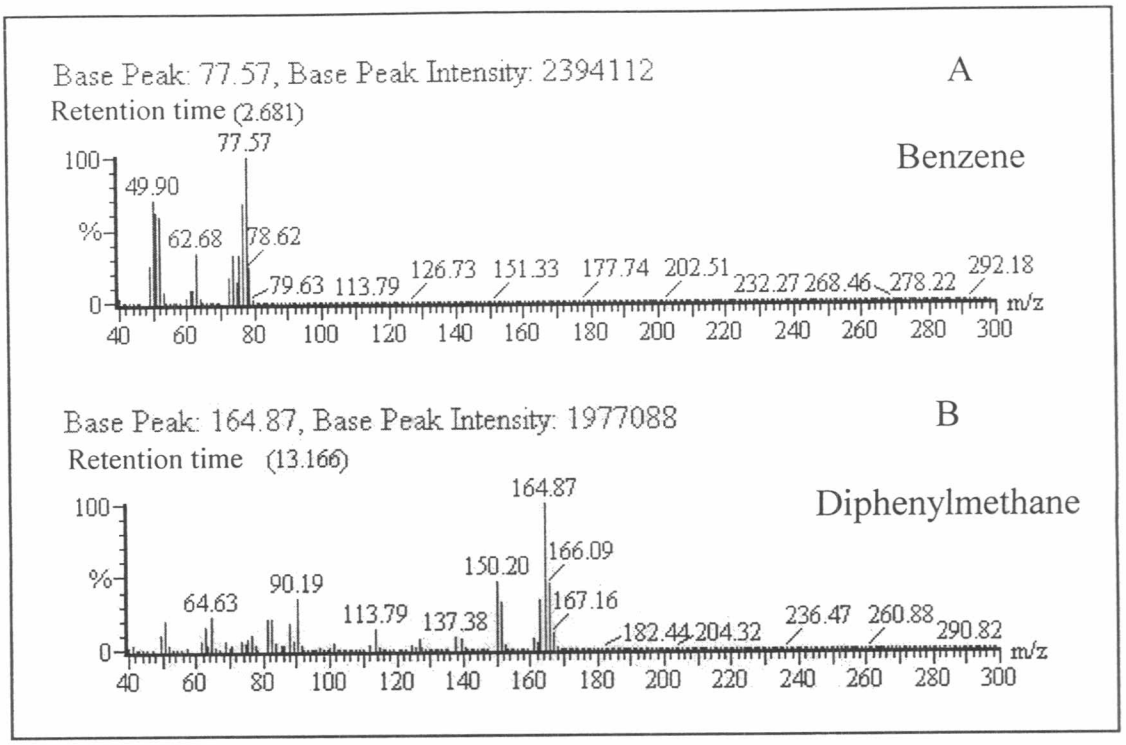

Figure 14.12 The mass spectra of benzene (A) and diphenylmethane (B)

4.3.2 Alkylation of Benzene with 2-chlorobutane Over Fe-MCM-41 Catalysts

The alkylation of benzene with 2-chlorobutane to produce *sec*-butylbenzene is another method for testing the catalytic performance of the Fe-MCM-41 samples. Figure 4.13 and 4.14 show the conversion of 2-chlorobetane and selectivity to *sec*-butylbenzene using Fe-MCM-41 synthesized from iron oxide waste and ferric nitrate, respectively. The conversion is increased with increasing the reaction time and temperature as the previous reaction. The high conversion up to 75 % is observed when the reaction is performed at 100 °C for 4 hours. Conversely, the selectivity to *sec*-butyl benzene is decreased when the temperature is raised. The highest selectivity is 82 % when Fe-MCM-41-NW4 is used as the catalyst. However, the polyalkylation is found and generated by product of di-*sec*-butylbenzene isomers. As shown in Figure 14.15A, the parents peak of sec-butylbenzene molecule is observed at m/z = 133.70 and the fragment peak

at m/z = 104 is assigned to the ion of ethylbenzene. Figure 14.15B and C show parents peak at m/z = 187.79 that referred to the ion of di-*sec*-butyl benzene isomers.

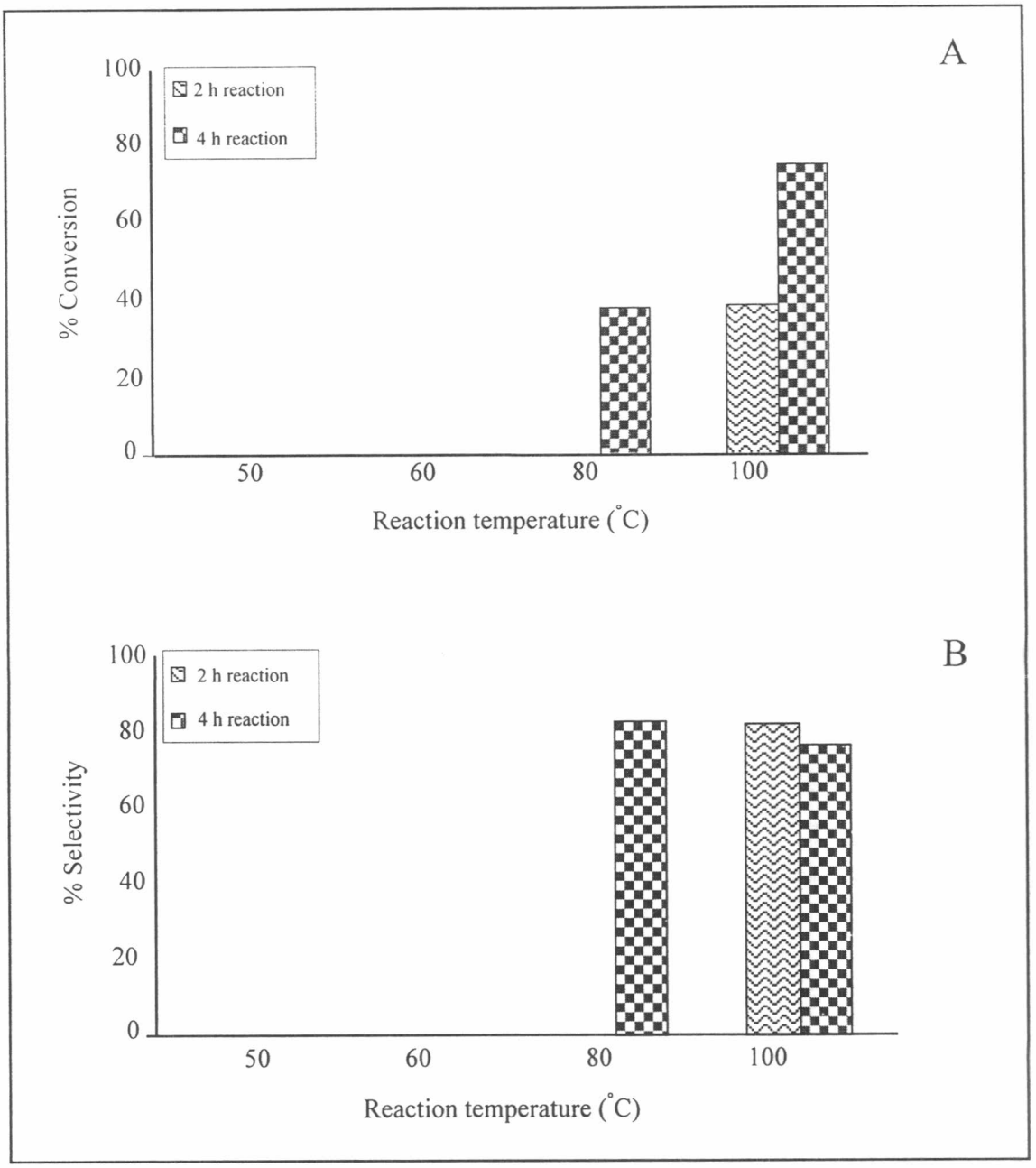

Figure 4.13 Catalytic activity of Fe-MCM-41-NW4 for alkylation of benzene with 2-chlorobutane; (A) Conversion of 2-chlorobutane and (B) Selectivity to *sec*-butylbenzene

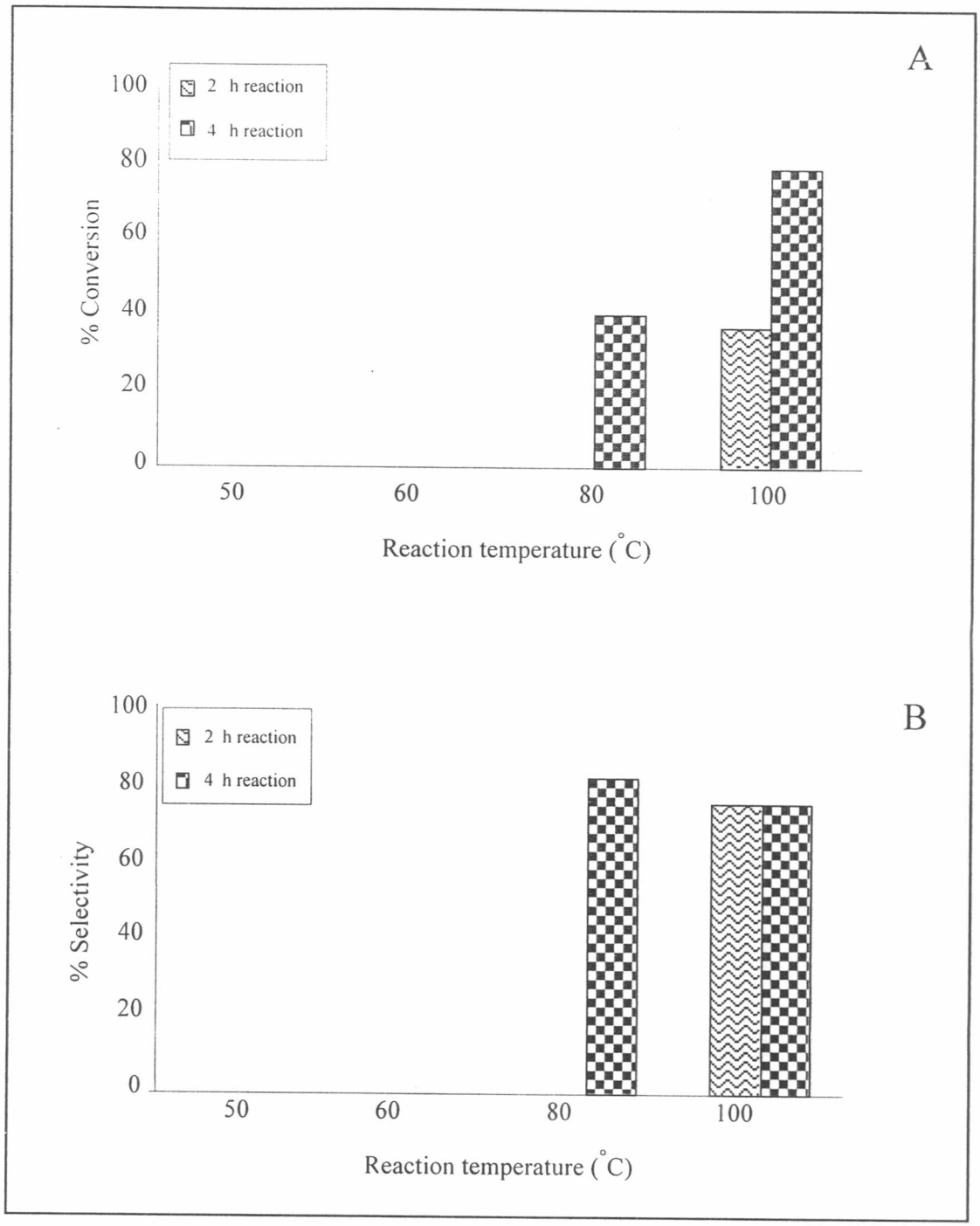

Figure 4.14 Catalytic activity of Fe-MCM-41-N4 for alkylation of benzene with 2-chlorobutane; (A) Conversion of 2-chlorobutane and (B) Selectivity to. *sec*-butylbenzene

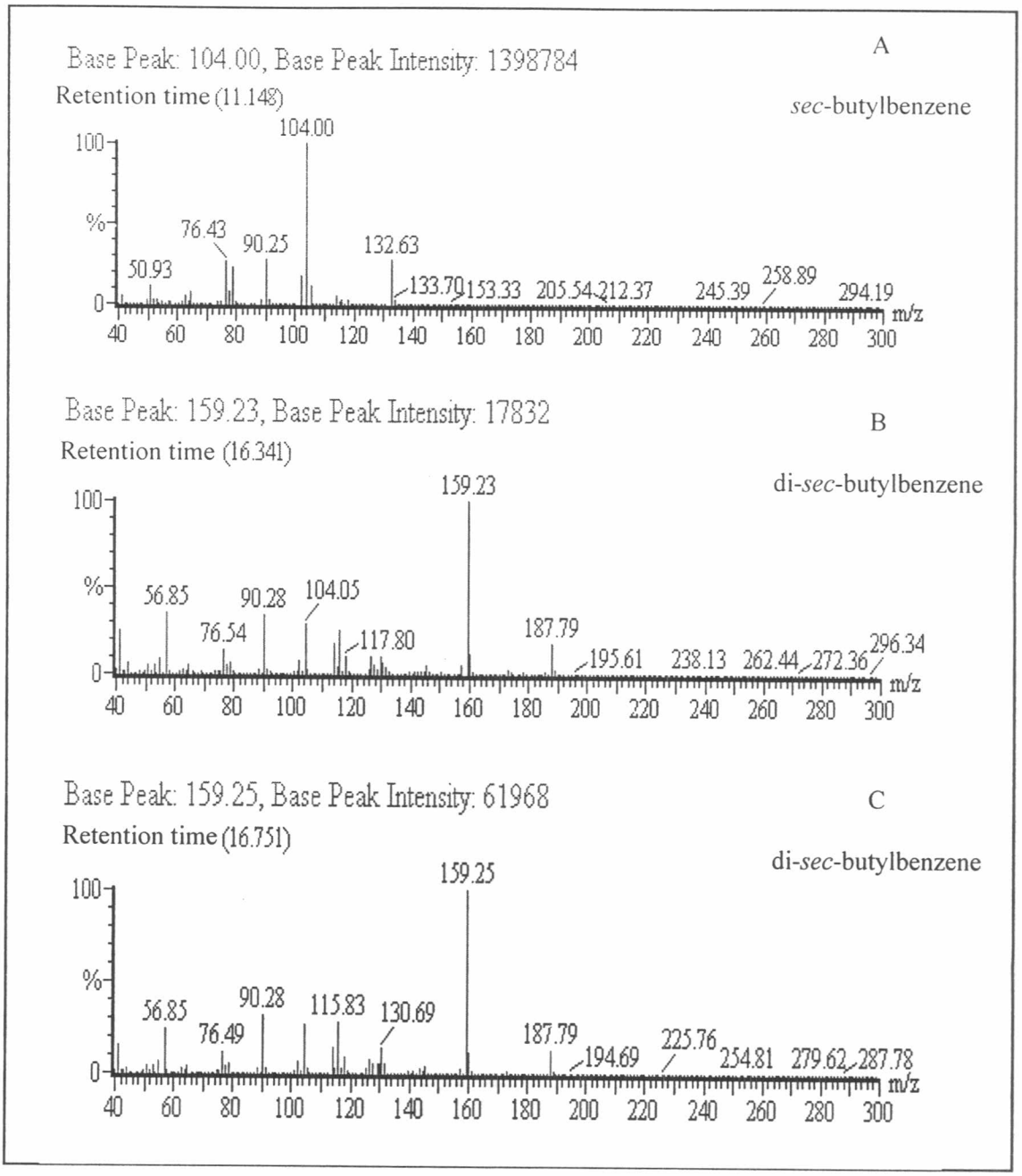

Figure 14.15 The mass spectra of *sec*-butylbenzene (A) and its by products, di-*sec*-butylbenzene (B, C)